

May 31, 2021

Phonon-driven ultrafast exciton dissociation at donor-acceptor polymer heterojunctions

Hiroyuki Tamura,[†] John G. S. Ramon,[‡] Eric R. Bittner,[‡] and Irene Burghardt[†]

[†]*Département de Chimie, Ecole Normale Supérieure,
24 rue Lhomond, F-75231 Paris cedex 05, France*

[‡]*Department of Chemistry and Texas Center for Superconductivity,
University of Houston, Houston, Texas 77204, USA*

Abstract

A quantum-dynamical analysis of phonon-driven exciton dissociation at polymer heterojunctions is presented, using a hierarchical electron-phonon model parameterized for three electronic states and 24 vibrational modes. Two interfering decay pathways are identified: a direct charge separation, and an indirect pathway via an intermediate bridge state. Both pathways depend critically on the dynamical interplay of high-frequency C=C stretch modes and low-frequency ring-torsional modes. The ultrafast, highly non-equilibrium dynamics is consistent with time-resolved spectroscopic observations.

PACS numbers: 78.55.Kz, 78.66.Qn, 31.70.Hq, 31.50.Gh

Semiconducting π -conjugated polymers are promising low-cost and flexible materials for electronic devices such as organic light-emitting diodes (OLEDs) and solar cells [1–3]. Many of the unique properties of these materials stem from the combination of the molecular structure of their building blocks and the extended nature of the π -system. Thus, excitonic states, i.e., electron-hole quasi-particle states that extend over the polymer strands, play a central role for the optoelectronic properties [3]. Exciton formation can result from polaron recombination, e.g., in OLEDs, or else from the primary photoexcitation step, e.g., in photovoltaic systems.

A key feature of organic semiconductors is the strong coupling between the elementary electronic processes and the material’s phonon modes [3,4] – much stronger than in inorganic semiconductors. This is underscored by experimental observations of sub-picosecond scale coherent nuclear motions following photoexcitation [5]. Further, the ultrafast nature of the electronic decay processes [6–8] suggests the presence of coherent vibronic coupling mechanisms, possibly determined by conical intersection topologies – very similar to the photophysics of polyatomic molecules and to Jahn-Teller effects in solids [9,10]. These observations call for a microscopic-level, quantum-dynamical interpretation of the basic charge and energy transfer processes.

In this Letter, we focus on the role of electron-phonon coupling in the charge transfer processes at bulk polymer heterojunctions [11]; these provide conditions for an extremely efficient charge separation at the interface between different phase-segregated polymers. The primary excitation is a photogenerated exciton stabilized by the electron-hole Coulombic interaction (with a typical binding energy of $\epsilon_B \sim 0.5$ eV [2]). Due to the highly folded interfacial area in bulk heterojunctions, the exciton has a high probability of reaching the interface within the diffusion length (typically ~ 20 nm). The exciton decay towards a charge-separated state (“exciplex”) is largely determined by molecular-level electronic in-

teractions at the interface. To a first approximation, the efficiency of charge generation depends on the ratio between ϵ_B and the band offset between the two polymer species [11, 12]. Recent time-resolved photoluminescence studies have shown that the exciton decay – and possible exciton regeneration – fall into a (sub)picosecond regime [7, 8]. While the elementary processes at the polymer interface are crucial for the device function and optimization, these processes are not well characterized as yet on the microscopic side. Against this background, the purpose of this Letter is to present a realistic quantum-dynamical model involving several electronic states and an explicit representation of the phonon distribution.

We specifically consider a heterojunction composed of the poly[9,9-dioctylfluorene-co-bis-N,N-(4-butyl-phenyl)-bis-N,N-phenyl-1,4-phenylenediamine] (TFB) and poly[9,9-dioctylfluorene-co-benzothiadiazole] (F8BT) polymer components [7, 12–14]. At the TFB:F8BT heterojunction, ϵ_B is found to be similar to the band offset, so that both exciton decay and regeneration phenomena are expected to occur. Semi-empirical calculations were used to identify the relevant electronic states and parameterize the vibronic coupling Hamiltonian used below (see Eq. (1)) for 24 explicit phonon modes covering the high-frequency (C=C stretch) and low-frequency (ring-torsional) phonon branches [13, 15, 16]. The exciton state (XT), which is the lowest excited state with significant oscillator strength, mainly has electron-hole density on the F8BT moiety, while the lowest-lying interfacial charge transfer state (CT) corresponds to a TFB⁺-F8BT⁻ charge separated state. (However, the CT state is not purely polaronic since it does carry oscillator strength to the ground state through mixing with excitonic configurations on the F8BT moiety). Among the manifold of remaining states, one is found to exhibit a strong coupling to the XT state [13]; this state will be considered as an intermediate state (IS) in the following, see Fig. 1.

To interpret the nonadiabatic decay of the exciton state, we apply a three-state vibronic coupling model in conjunction with highly accurate wavepacket propagation techniques,

i.e., the multiconfiguration time-dependent Hartree (MCTDH) method [17]. In particular, we use a linear vibronic coupling (LVC) model [9] which is appropriate in view of the moderate nuclear displacements during the process. The N -mode LVC Hamiltonian (here, $N=24$) reads as follows, using mass and frequency weighted coordinates and atomic units ($\hbar = 1$),

$$\mathbf{H} = \sum_{i=1}^N \frac{\omega_i}{2} (p_i^2 + x_i^2) \mathbf{1} + \sum_{i=1}^N \begin{pmatrix} \kappa_i^{(1)} x_i & \lambda_i^{(12)} x_i & \lambda_i^{(13)} x_i \\ \lambda_i^{(12)} x_i & \kappa_i^{(2)} x_i & \lambda_i^{(23)} x_i \\ \lambda_i^{(13)} x_i & \lambda_i^{(23)} x_i & \kappa_i^{(3)} x_i \end{pmatrix} + \mathbf{C} \quad (1)$$

Here, $\mathbf{1}$ and \mathbf{C} denote the unit matrix and a coordinate independent constant matrix, respectively; the ω_i , $p_i = -i\partial/\partial x_i$, and x_i are the frequencies, momenta, and displacements along the vibrational normal modes. The diagonal and off-diagonal potential terms correspond to the diabatic potentials and couplings. The model Eq. (1) allows for the presence of conical intersections between pairs of electronic states at nuclear configurations where the diabatic coupling vanishes and the adiabatic states become degenerate [9].

We further apply a recently developed effective-mode representation of the LVC model [18], which separates the Hamiltonian into effective-mode vs. residual-mode parts,

$$\mathbf{H} = \mathbf{H}_{\text{eff}} + \mathbf{H}_{\text{res}} \quad (2)$$

By an orthogonal coordinate transformation, $\mathbf{X} = \mathbf{T}\mathbf{x}$, a subset of effective modes is generated which subsume all vibronic coupling terms of an electronic N_s -state system into $\frac{1}{2}N_s(N_s + 1)$ effective modes [18]. This construction, which was previously applied to two-state systems (three effective modes) [16, 18, 19], is here extended for the first time to three electronic states (six effective modes),

$$\begin{aligned} \mathbf{H}_{\text{eff}} = & \sum_{i=1}^6 \frac{\Omega_i}{2} (P_i^2 + X_i^2) \mathbf{1} + \sum_{i=1}^6 \begin{pmatrix} (K_i + D_i) X_i & \Lambda_i^{(12)} X_i & \Lambda_i^{(13)} X_i \\ \Lambda_i^{(12)} X_i & (K_i - D_i) X_i & \Lambda_i^{(23)} X_i \\ \Lambda_i^{(13)} X_i & \Lambda_i^{(23)} X_i & K_i^{(3)} X_i \end{pmatrix} \\ & + \sum_{i=1}^6 \sum_{j=i+1}^6 d_{ij} (P_i P_j + X_i X_j) \mathbf{1} + \mathbf{C} \end{aligned} \quad (3)$$

where the parameters and modes \mathbf{X} are defined by extension of the two-state construction described in Refs. [16, 18]. Two of the six effective modes (i.e., X_1 and X_2) are chosen as topology-adapted modes which span the branching plane [20] for a given pair of electronic states (here, states 1 and 2), i.e., the plane along which the degeneracy at the conical intersection is lifted, see Fig. 2. Several of the coupling constants in Eq. (3), i.e., the $\Lambda_i^{(12)}$ ($i \geq 2$), D_i ($i \geq 3$), K_i ($i = 4, 5, 6$), $\Lambda_i^{(12)}$ ($i = 5, 6$), and $\Lambda_6^{(13)}$, are zero by construction.

The residual modes, X_i , $i = 7, \dots, N$, do not couple directly to the electronic subsystem, but couple bilinearly to the effective modes. By analogy with our recent two-state analysis [16], \mathbf{H}_{res} can be transformed to a band-diagonal structure, yielding the n th-order Hamiltonian

$$\mathbf{H}^{(n)} = \mathbf{H}_{\text{eff}} + \sum_{l=1}^n \mathbf{H}_{\text{res}}^{(l)} \quad (4)$$

where each l th-order residual term comprises 6 modes,

$$\mathbf{H}_{\text{res}}^{(l)} = \sum_{i=6l+1}^{6l+6} \frac{\Omega_i}{2} (P_i^2 + X_i^2) \mathbf{1} + \sum_{i=6l+1}^{6l+6} \sum_{j=i-6}^{i-1} d_{ij} (P_i P_j + X_i X_j) \mathbf{1} \quad (5)$$

For $6 + 6n = N$, the n th-order Hamiltonian $\mathbf{H}^{(n)}$ is equivalent to the original Hamiltonian Eq. (1).

We refer to Eqs. (2)-(3) in conjunction with Eqs. (4)-(5) as a hierarchical electron-phonon (HEP) model [16, 19]. Successive orders of the HEP Hamiltonian can be shown to conserve the moments (cumulants) of the original Hamiltonian up to the $(2n+3)$ rd order [16]. Truncation of the HEP Hamiltonian creates a series of reduced dimensionality models, associated with approximate n th-order propagators which accurately reproduce the dynamics of the overall system up to a certain time. While the lowest-order description – \mathbf{H}_{eff} only – can be appropriate, e.g., for a rapid passage through a conical intersection region [18], the present system will be shown to necessitate a higher-order analysis.

The effective-mode construction for the TFB:F8BT heterojunction shows that \mathbf{H}_{eff} is essentially determined by high-frequency C=C stretch modes while $\mathbf{H}_{\text{res}}^{(1)}$ is determined by

low-frequency ring torsional modes. This is analogous to our previous analysis of a two-state XT-CT model [16]. Importantly, the low-frequency modes will be shown to play a key role in generating the observed ultrafast exciton decay.

Fig. 2 shows the diabatic XT, CT, and IS potential energy surfaces (PES), for a cut through the XT-CT branching plane defined in terms of the effective modes $(X_1, X_2)_{\text{XT,CT}}$, and an alternative representation involving the XT-IS branching plane spanned by another set of effective modes $(X'_1, X'_2)_{\text{XT,IS}}$. As can be inferred from the figure, the exciton dissociation process is determined by a landscape of multiple intersecting surfaces, and the branching plane topology is a key factor in the nonadiabatic dynamics. Of particular interest for the present analysis is the role of the intermediate state (IS) that lies above the exciton state but could be accessible due to its strong diabatic coupling to the XT state, and due to the significant extension of the wavepacket.

Fig. 3a shows the population evolution obtained from MCTDH simulations for the overall 3-state, 24-mode system according to Eq. (1). An ultrafast initial $\text{XT} \rightarrow \text{CT}$ decay takes place ($\sim 50\%$ at 150 fs), followed by an oscillatory behavior of the XT and CT populations which is found to persist over the 3 picosecond observation interval. These observations are in qualitative agreement with the experimentally observed exciton decay and regeneration [7], even though a steady overall increase of the CT population is eventually observed in our simulation. The IS population experiences an initial increase, but does not rise above an average of $\sim 10\%$ beyond 500 fs. Yet, one cannot exclude the possibility that this state acts as a “bridge” facilitating the XT-CT transfer.

To investigate the possibility of an exciton decay pathway via the IS state, $\text{XT} \rightarrow \text{IS} \rightarrow \text{CT}$, we set the XT-CT diabatic coupling artificially to zero, such that only the indirect pathway is permitted. As can be inferred from Fig. 3b, a subpicosecond exciton decay and concomitant rise of the CT state population is also observed in this case, even though the process is somewhat slower than in the fully coupled 3-state dynamics. Again, the IS

population tends towards an average of $\sim 10\%$, i.e., the IS state facilitates the XT-CT transition but does not act as an additional acceptor state. Overall, the dynamics of Fig 2a is therefore the result of a superposition of the direct (XT \rightarrow CT) and indirect (XT \rightarrow IS \rightarrow CT) pathways. Given that the XT \rightarrow IS transfer is endothermic (with a ~ 0.2 eV barrier) in a conventional kinetic picture, the efficiency of the indirect pathway is entirely a consequence of the quantum dynamical character of the process.

The remaining part of the analysis addresses the HEP construction of Eqs. (2)-(5), with the twofold objective of identifying a reduced-dimensionality picture of the dynamics, and understanding the role of the different types of phonon modes, i.e., high-frequency C=C stretch modes (constituting \mathbf{H}_{eff}) vs. low-frequency ring-torsional modes (constituting $\mathbf{H}_{\text{res}}^{(1)}$). As shown in Fig. 4, the high-frequency modes by themselves, at the level of the 6-mode $\mathbf{H}^{(0)}$ approximation, cannot reproduce the exciton decay (even though they correctly reproduce the shortest-time dynamics, on the order of 50 fs). At this level of approximation, quantum phase coherence effects are substantially overestimated, leading to a weak, periodic population transfer. By contrast, inclusion of the low-frequency modes, at the level of the 12-mode $\mathbf{H}^{(1)}$ approximation, results in a qualitatively correct description of the dynamics. Indeed, the low-frequency modes induce vibrational energy redistribution and dephasing effects that eventually lead to an irreversible exciton decay. Finally, the $\mathbf{H}^{(2)}$, 18-mode approximation is essentially identical to the exact, 24-mode result on a ~ 1 ps time scale. A similar interpretation holds for the indirect pathway in the absence of XT-CT coupling. All of these results would carry over to an initial parameterization involving a very large number N of phonon modes, e.g., thousands of modes. While dynamical calculations according to Eq. (1) would not be feasible for such a “macrosystem”, the HEP model gives a correct reduced-dimensionality description of the ultrafast dynamics.

In summary, we present the results of fully quantum dynamical calculations of a model polymer heterojunction interface. In particular, we highlight the role that intermediate

states may play in the overall XT \rightarrow CT conversion. While these results go significantly beyond our earlier interpretation for a two-state model [16], the key role of the low-frequency modes is confirmed, pointing to the generic nature of the observed dynamical pattern for a two-band phonon distribution (see also Refs. [4,21] which address the spectroscopic signature of both types of phonon modes in phenylene based polymers). Our analysis highlights the coherent, quantum-dynamical character of the process, and the importance of the multidimensional topology. Thus, the branching plane of Fig. 2 replaces the conventional Marcus parabola picture [22], and the HEP model provides the correct reduced-dimensionality dynamics on short time scales. Extensions of the present analysis concern (i) the inclusion of temperature effects, and (ii) the improvement of the present parameterization, along with the generalization to multiple electronic states that potentially appear in the role of bridge states. The positions of such states relative to the XT and CT states and their electronic properties are indeed quite sensitive to the local morphology and packing geometries of the respective polymers at the interface as indicated by recent time-dependent density functional theory [14] and semi-empirical investigations [23]. Consequently, the extent to which such intermediate states will play a role will depend on the local morphology of the interface and the actual physical system will be an ensemble of individual cases. Using this local, molecular-level information, the HEP approach should contribute to a realistic modeling of the highly nonequilibrium exciton decay processes in extended π -conjugated systems.

We thank Andrey Pereverzev, Etienne Gindensperger, and Lorenz Cederbaum for constructive discussions. This work was supported by the ANR-05-NANO-051-02 and ANR-NT05-3-42315 projects, by NSF grant CHE-0345324, and by the Robert Welch Foundation.

References

¹R. H. Friend et al., *Nature* **397**, 121 (1999); M. Granström et al., *Nature* **395**, 257 (1998); L. Schmidt-Mende et al., *Science* **293**, 1119 (2001); J. L. Bredas, D. Beljonne, V. Coropceanu, and J. Cornil, *Chem. Rev.* **104**, 4971 (2004); S. Günes, H. Neugebauer, and N. S. Sariciftci, *Chem. Rev.* **107**, 1324 (2007).

²J. J. M. Halls et al., *Phys. Rev. B* **60**, 5721 (1999).

³G. D. Scholes and G. Rumbles, *Nature Materials* **5**, 683 (2006).

⁴S. Tretiak, A. Saxena, R. L. Martin, and A. R. Bishop, *Phys. Rev. Lett.* **89**, 097402 (2002).

⁵G. Lanzani, G. Cerullo, C. Brabec, and N. S. Sariciftci, *Phys. Rev. Lett.* **90**, 047402 (2003).

⁶R. Kersting et al., *Phys. Rev. Lett.* **70**, 3820 (1993).

⁷A. C. Morteani, P. Sreearunothai, L. M. Herz, R. H. Friend, and C. Silva, *Phys. Rev. Lett.* **92**, 247402 (2004).

⁸X. Ai, M. C. Beard, K. P. Knutsen, S. E. Shaheen, G. Rumbles, and R. E. Ellingson, *J. Phys. Chem. B*, **110**, 25462 (2006).

⁹H. Köppel, W. Domcke, and L. S. Cederbaum, *Adv. Chem. Phys.* **57**, 59 (1984); I. B. Bersuker and V. Z. Polinger, 1989, *Vibronic Interactions in Molecules and Crystals*, Springer Series in Chemical Physics, 1989.

¹⁰H. Nakamura, *Nonadiabatic Transition: Concepts, Basic Theories and Applications*, World Scientific, Singapore, 2002; *Conical Intersections*, ed. W. Domcke, D. R. Yarkony, and H. Köppel, World Scientific, New Jersey, 2004, Vol. 15, p. 323.

- ¹¹G. Yu, J. Gao, J. C. Hummelen, F. Wudl, and A. J. Heeger, *Science* **270**, 1789 (1995); J. J. M. Halls, C. A. Walsh, N. C. Greenham, E. A. Marseglia, R. H. Friend, S. C. Moratti, and A. B. Holmes, *Nature* **376**, 498 (1995).
- ¹²E. R. Bittner, J. Ramon, and S. Karabunarliev, *J. Chem. Phys.* **122**, 214719 (2005); E. R. Bittner and J. Ramon, in *Quantum Dynamics of Complex Molecular Systems*, eds. I. Burghardt and D. A. Micha, Springer, Heidelberg, 2006.
- ¹³J. Ramon and E. R. Bittner, *J. Phys. Chem. B* **110**, 21001 (2006).
- ¹⁴J. Ramon and E. R. Bittner, *J. Chem. Phys.* **126**, 181101 (2007).
- ¹⁵A. Pereverzev and E. R. Bittner, *J. Chem. Phys.* **125**, 104906 (2006).
- ¹⁶H. Tamura, E. R. Bittner, and I. Burghardt, *J. Chem. Phys.* **126**, 21103 (2007); *J. Chem. Phys.* in press.
- ¹⁷H.-D. Meyer, U. Manthe, and L. S. Cederbaum, *Chem. Phys. Lett.* **165**, 73 (1990); M. H. Beck, A. Jäckle, G. A. Worth, and H.-D. Meyer, *Phys. Rep.* **324**, 1 (2000).
- ¹⁸L. S. Cederbaum, E. Gindensperger, and I. Burghardt, *Phys. Rev. Lett.* **94**, 113003 (2005); E. Gindensperger, I. Burghardt, and L. S. Cederbaum, *J. Chem. Phys.* **124**, 144103 (2006); I. Burghardt, E. Gindensperger, and L. S. Cederbaum, *Mol. Phys.* **104**, 1081 (2006).
- ¹⁹E. Gindensperger, H. Köppel, and L. S. Cederbaum, *J. Chem. Phys.* **126**, 34106 (2007).
- ²⁰G. J. Atchity, S. S. Xantheas, and K. Ruedenberg, *J. Chem. Phys.* **95**, 1862 (1991).
- ²¹S. Karabunarliev, E. R. Bittner, and M. Baumgarten, *J. Chem. Phys.* **114**, 5863 (2001).
- ²²R. A. Marcus, *Rev. Mod. Phys.* **65**, 599 (1993).
- ²³P. Sreearunothai, A. C. Morteani, I. Avilov, J. Cornil, D. Beljonne, R. H. Friend, R. T. Phillips, C. Silva and L. M. Herz, *Phys. Rev. Lett.* **96**, 117403 (2006).

Figure legends

Fig. 1. (Color online) Schematic illustration of (a) the TFB:F8BT donor-acceptor heterojunction and (b) the photoexcitation process and potential crossings. The blue, red, and purple lines indicate the XT, CT, and IS diabatic potentials, respectively. (Dotted lines indicate the corresponding adiabatic potentials.) The red and purple arrows indicate the direct $\text{XT} \rightarrow \text{CT}$ vs. indirect $\text{XT} \rightarrow \text{IS} \rightarrow \text{CT}$ exciton dissociation pathways.

Fig. 2. (Color online) Branching-plane projections of the coupled diabatic PESs: (a) XT, CT and IS PESs projected onto the XT-CT branching plane, and (b) XT and IS PESs projected onto the XT-IS branching plane; here, the wavepacket width and trajectory of the wavepacket center (blue arrow) are also indicated. (These branching space projections are associated with two different sets of effective modes \mathbf{X} .) The white, blue, red and purple circles indicate the conical intersection, the minima on the XT, CT and IS states, respectively. The dotted lines indicate the avoided-crossing seam lines.

Fig. 3. (Color online) Time-evolving state populations for (a) the full 3-state 24-mode wavepacket propagation, and (b) a complementary 3-state 24-mode calculation where the indirect ($\text{XT} \rightarrow \text{IS} \rightarrow \text{CT}$) pathway was selected by setting the XT-CT diabatic coupling to zero.

Fig. 4. (Color online) CT populations for the truncated HEP Hamiltonian $\mathbf{H}^{(n)}$ of Eq. (4), for $n = 0$ (6 modes), $n = 1$ (12 modes), and $n = 2$ (18 modes), as compared with the exact 24-mode result.

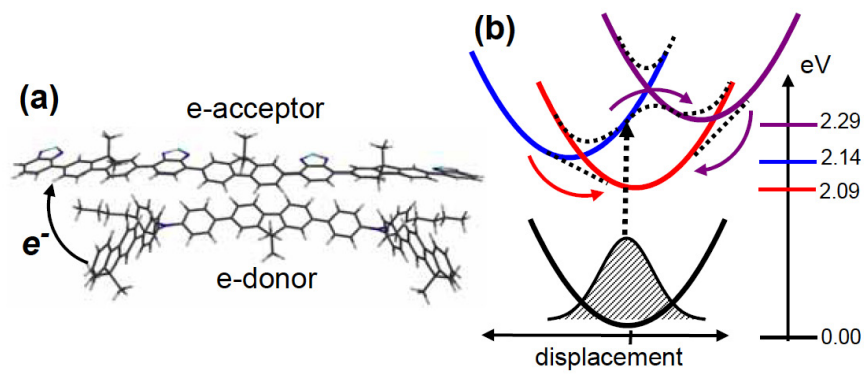


Fig. 1

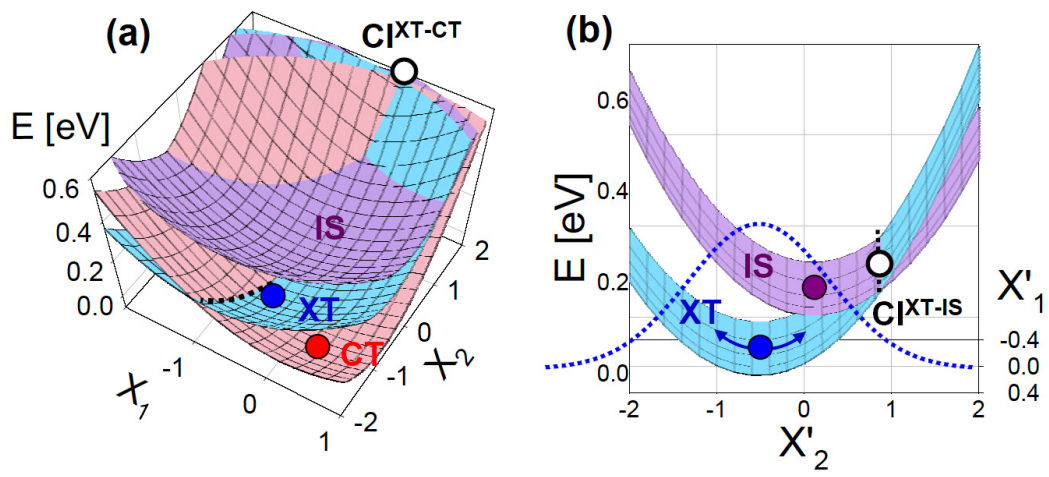


Fig. 2

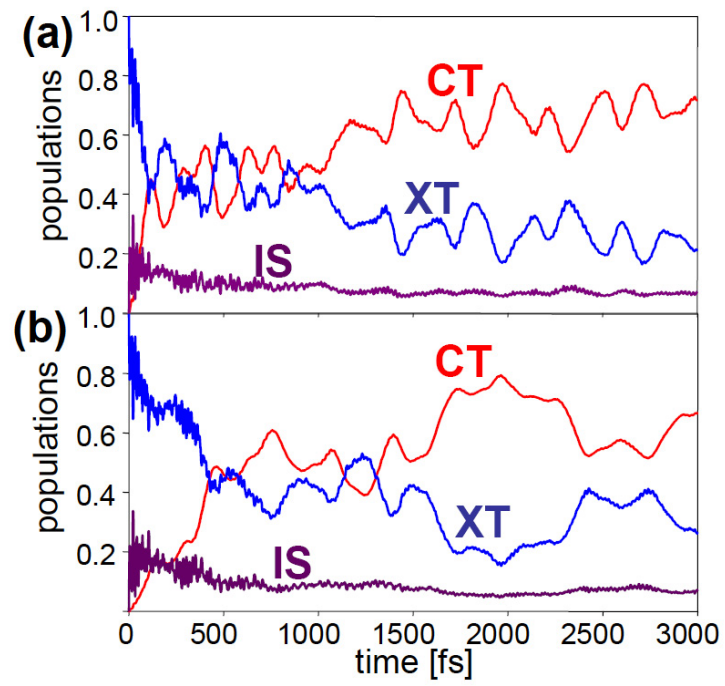


Fig. 3

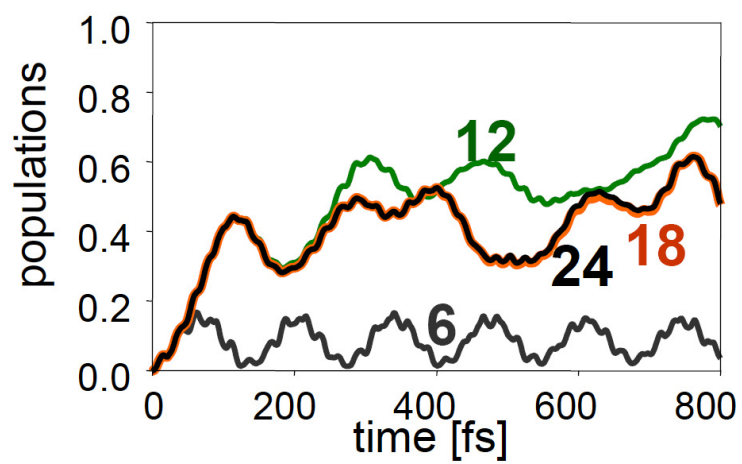


Fig. 4